

C-axis Raman spectra of a normal plane-chain bilayer cuprate and the pseudogap

W. C. Wu and J. P. Carbotte

Department of Physics and Astronomy, McMaster University

Hamilton, Ontario, Canada L8S 4M1

(March 31, 2018)

Abstract

We investigate the Raman spectra in the geometry where both incident and scattered photon polarizations are parallel to the \hat{z} -direction, for a plane-chain bilayer coupled via a single-particle tunneling t_{\perp} . The Raman vertex is derived in the tight-binding limit and in the absence of Coulomb screening, the Raman intensity can be separated into intraband ($\propto t_{\perp}^4$) and interband ($\propto t_{\perp}^2$) transitions. In the small- t_{\perp} limit, the interband part dominates and a pseudogap will appear as it does in the conductivity. Coulomb interactions bring in a two-particle coupling and result in the breakdown of intra- and interband separation. Nevertheless, when t_{\perp} is small, the Coulomb screening ($\propto t_{\perp}^4$) has little effect on the intensity to which the unscreened interband transitions contribute most. In general, the total Raman spectra are strongly dependent on the magnitude of t_{\perp} .

PACS numbers: 74.80.Dm, 78.30.-j, 74.25.Jb, 74.72.-h

Typeset using REVTeX

I. INTRODUCTION

Recently, c -axis properties of the high- T_c superconductors have been of increasing interest both in normal and superconducting states. Among several theoretical works [1–8], a coupled plane-chain model has been proposed [9,10] to study various c -axis properties of YBaCuO. Due to a coupling (of magnitude t_\perp) between plane and chain along the c -axis, the properties in the c -direction are shown to be quite different as compared to the ones in the a - b plane. More importantly, a finite band gap (splitting) between the two renormalized bands (arising from the finite coupling) gives a natural explanation of pseudogaps, which are mainly observed in the underdoped normal-state copper oxides [11–13] and are seen directly as a depression of the conductivity at low frequency at low temperatures.

In the past few years, Raman scattering as a probe to study high T_c materials have been very successful [14–27] and have in particular played a significant role in the debate about the symmetry of the gap. Owing to the layer behavior of the high T_c compounds, most experimental and theoretical studies have focused on the a - b plane properties, taking into account different symmetrical geometries. In contrast in this paper, we want specially to study the c -axis normal-state Raman scattering, based on the coupled plane-chain bilayer model. This not only provides another way to test whether this model is valid in high T_c cuprates, but also gives a path for extending calculations from a simple one band system to the more complicated multiband system. In particular, a better theory should take Coulomb interactions into account properly for a multiband system.

Devereaux *et al.* [28] have recently given a detailed account of Raman scattering in a superconducting bilayer with two identical planes. They use the effective mass approximation to derive the Raman vertex and have mainly studied the a - b plane properties. In their calculations, they have ignored the interband transition which is not so important in the a - b plane, but turns out to be the dominant part in some cases for the c -axis. This case is discussed in the present paper.

A summary of what we have done is as follows. We have derived the Raman vertex

in the tight-binding limit which is almost exact in a single bilayer limit. We have clearly exhibited in the c -axis Raman spectra, the role of the intra- and interband transitions which are separable in the absence of the Coulomb screening. The interband transitions contribute most in the small- t_{\perp} limit. While a mixing term comes in when the Coulomb screening is included, the unscreened interband transition still dominates if t_{\perp} is small. Appendix A gives the details of how one can separate the response functions needed in the calculation of the Raman spectra into intraband and interband contributions. In Appendix B, we present the analogous results for the c -axis Raman spectra in the case of a plane-plane bilayer model. In this instance, a simple analytic end expression can be obtained which helps gain physical insight into the c -axis Raman process. The total volume has been set to one ($\Omega = 1$) in this paper.

II. FORMALISM

The non-interacting Hamiltonian for the normal state of a coupled plane-chain bilayer cuprate is written as

$$H_0 = \sum_{\mathbf{k}} C_{\mathbf{k}}^{\dagger} h(\mathbf{k}) C_{\mathbf{k}}, \quad (1)$$

where we have defined the row and column vectors

$$C_{\mathbf{k}}^{\dagger} = (c_{1\mathbf{k}}^{\dagger}, c_{2\mathbf{k}}^{\dagger}) \quad ; \quad C_{\mathbf{k}} = \begin{pmatrix} c_{1\mathbf{k}} \\ c_{2\mathbf{k}} \end{pmatrix}, \quad (2)$$

and $c_{1\mathbf{k}}^{\dagger}, c_{2\mathbf{k}}^{\dagger}$ create an electron in the state \mathbf{k} in layers 1 and 2 respectively. The energy matrix

$$h(\mathbf{k}) = \begin{pmatrix} \xi_1(\mathbf{k}) & t(k_z) \\ t(k_z) & \xi_2(\mathbf{k}) \end{pmatrix}. \quad (3)$$

Here ξ_1 and ξ_2 are the (uncoupled) energy bands for the plane and chain respectively and t (assumed to be real) is the perpendicular hopping coupling between plane and chain. These quantities are defined explicitly later in Eq. (22). The spin indices are suppressed throughout this paper.

To study the Raman spectra for a multiband system, we use an approach which is suitable in the tight-binding limit. The Hamiltonian (1) can be written in the Wannier representation as [29]

$$H_0 = - \sum_{i=1}^2 \sum_{\mathbf{R}_i, \mathbf{r}_i} \sigma_i c_i^\dagger(\mathbf{R}_i + \mathbf{r}_i) c_i(\mathbf{R}_i) - \frac{t_\perp}{2} \sum_{\mathbf{R}_1, \mathbf{R}_2} \left\{ c_1^\dagger(\mathbf{R}_1) c_2(\mathbf{R}_2) [\delta_{\mathbf{R}_1 + \hat{z}d/2, \mathbf{R}_2} + \delta_{\mathbf{R}_1 - \hat{z}d/2, \mathbf{R}_2}] + \text{H.c.} \right\}, \quad (4)$$

where \mathbf{R}_i are the lattice vectors in a plane, \mathbf{r}_i are the displacements to the nearest neighbors of \mathbf{R}_i , d is the lattice constant in the z direction, and σ_i and t_\perp are the nearest-neighbor hopping energies within and between the chain and plane layers. The Wannier representation is connected to the \mathbf{k} -space representation by

$$c_i(\mathbf{R}_i) = \frac{1}{\sqrt{N}} \sum_{\mathbf{k}} e^{i\mathbf{k} \cdot \mathbf{R}_i} c_i(\mathbf{k}), \quad (5)$$

where N is the total number of lattice sites. In the presence of a magnetic vector potential $\mathbf{A}(\mathbf{r})$, the tight-binding Wannier states are modified by a phase such that [30]

$$c_i(\mathbf{R}_i) \rightarrow c_i(\mathbf{R}_i) \exp \left[-\frac{ie}{\hbar c} \mathbf{R}_i \cdot \mathbf{A}(\mathbf{R}_i) \right], \quad (6)$$

where e is the charge on the electron, \hbar is Planck's constant over 2π , and c is the speed of light. The assumption is made that the vector potential is slowly varying over the length scale of the crystal lattice and hence $\mathbf{A}(\mathbf{q})$ is strongly peaked about $\mathbf{q} = 0$.

Substituting (5) and (6) into (4), to second order in \mathbf{A} , Eq. (4) becomes

$$H = H_0 - \frac{e}{2mc} \mathbf{p} \cdot \mathbf{A} + \frac{e^2}{2mc^2} \mathbf{A} \cdot \overleftrightarrow{\rho} \cdot \mathbf{A} \quad (7)$$

in the \mathbf{k} -space, where the vector

$$\mathbf{p} = \frac{m}{\hbar} \sum_{\mathbf{k}} C_{\mathbf{k}}^\dagger \frac{\partial h(\mathbf{k})}{\partial \mathbf{k}} C_{\mathbf{k}} \quad (8)$$

and the tensor

$$\overleftrightarrow{\rho} = \frac{m}{\hbar^2} \sum_{\mathbf{k}} C_{\mathbf{k}}^\dagger \frac{\partial^2 h(\mathbf{k})}{\partial \mathbf{k} \partial \mathbf{k}} C_{\mathbf{k}}. \quad (9)$$

In these formulas m is the bare electron mass. In electronic Raman scattering, we are interested in the transition matrix to order \mathbf{A}^2 . Therefore, the term $\mathbf{A} \cdot \overleftrightarrow{\rho} \cdot \mathbf{A}$ in (7) is used in first-order perturbation theory and the term $\mathbf{p} \cdot \mathbf{A}$ in (7) is used in second-order perturbation theory. As a result, Raman scattering probes an “effective density”

$$\tilde{\rho} \equiv \sum_{\mathbf{k}} C_{\mathbf{k}}^\dagger \gamma(\mathbf{k}) C_{\mathbf{k}}, \quad (10)$$

where the vertex matrix has the element

$$\begin{aligned} \gamma_{ij}(\mathbf{k}) = & (\hat{\mathbf{e}}^I \cdot \overleftrightarrow{\rho}_{ij} \cdot \hat{\mathbf{e}}^S) + \sum_l \left[\frac{\langle i, \mathbf{k} | \mathbf{p} \cdot \hat{\mathbf{e}}^S | l, \mathbf{k} \rangle \langle l, \mathbf{k} | \mathbf{p} \cdot \hat{\mathbf{e}}^I | j, \mathbf{k} \rangle}{\epsilon_j(\mathbf{k}) - \epsilon_l(\mathbf{k}) + \hbar\omega^I} \right. \\ & \left. + \frac{\langle i, \mathbf{k} | \mathbf{p} \cdot \hat{\mathbf{e}}^I | l, \mathbf{k} \rangle \langle l, \mathbf{k} | \mathbf{p} \cdot \hat{\mathbf{e}}^S | j, \mathbf{k} \rangle}{\epsilon_j(\mathbf{k}) - \epsilon_l(\mathbf{k}) - \hbar\omega^S} \right]. \end{aligned} \quad (11)$$

In Eq. (11), the summation is over all the uncoupled bands and the dependence of the momentum transfer \mathbf{q} on $\gamma_{\mathbf{k}}$ is dropped since we assume $q \ll k_F$ (the Fermi momentum). $\epsilon_i(\mathbf{k})$ is the energy of the i -band, $\hat{\mathbf{e}}^I$ ($\hat{\mathbf{e}}^S$) is the polarization of incident (scattered) photon, and the frequency ω^I (ω^S) denotes the incident (scattered) photon energy.

For the problem of a plane-chain bilayer, one has two bands. In the case that there is a band gap (Δ) between these two bands which is very small compared to the energies of incident and scattered photons, $\Delta \ll \omega^I, \omega^S$, the second term of (11) is negligible. The Raman vertex matrix in (10) thus reduces to

$$\gamma(\mathbf{k}) = \frac{m}{\hbar^2} \sum_{\mu, \nu} \hat{\mathbf{e}}^I_\mu \frac{\partial^2 h(\mathbf{k})}{\partial k_\mu \partial k_\nu} \hat{\mathbf{e}}^S_\nu. \quad (12)$$

Eq. (12) shows how one can study various geometries for the Raman spectra by choosing the appropriate incident and scattered photon polarizations. We note that while the vertices exhibited in (12) are somewhat similar to the vertex given by the famous “effective mass approximation” [31,28], the physical origin is different.

The differential cross section for Raman scattering is found to be [32]

$$\frac{d^2\sigma}{d\omega d\Omega} = \frac{1}{\pi} r_0^2 \frac{\omega^S}{\omega^I} [1 + n_B(\omega)] \text{Im} \chi_{\tilde{\rho}\tilde{\rho}}(\mathbf{q} \rightarrow 0, i\omega_n \rightarrow \omega + i0^+), \quad (13)$$

where $n_B(\omega) = [\exp(\beta\omega) - 1]^{-1}$ is the Bose distribution function; $r_0 = e^2/mc^2$ is the so-called Thompson radius, and the Raman density response function

$$\chi_{\tilde{\rho}\tilde{\rho}}(\mathbf{q}, i\omega_n) = - \int_0^\beta d\tau e^{i\omega_n\tau} \langle T_\tau \tilde{\rho}_{\mathbf{q}}(\tau) \tilde{\rho}_{\mathbf{q}}^\dagger(0) \rangle, \quad (14)$$

which is given in terms of the effective density operator $\tilde{\rho}$ given in Eq. (10). Taking into account the screening effect due to the Coulomb energy

$$H_c = \frac{1}{2} \sum_{\mathbf{q}} \sum_{i,j=1}^2 U_{ij}(\mathbf{q}) \rho_{i,\mathbf{q}} \rho_{j,\mathbf{q}}, \quad (15)$$

the Raman response function (14) in (13) will be replaced by [32–34]

$$\chi_{\tilde{\rho}\tilde{\rho}}^{\text{sc}} = \chi_{\tilde{\rho}\tilde{\rho}} + \sum_{ij=1}^2 \chi_{\tilde{\rho}\rho_i} U_{ij}(\mathbf{q}) \chi_{\rho_j\tilde{\rho}} + \sum_{ijml=1}^2 \chi_{\tilde{\rho}\rho_i} U_{ij}(\mathbf{q}) \chi_{\rho_j\rho_m} U_{ml}(\mathbf{q}) \chi_{\rho_l\tilde{\rho}} + \dots \quad (16)$$

Both the intralayer and interlayer Coulomb interactions should be included. Here the real density on layer i is

$$\rho_{i,\mathbf{q}} = \sum_{\mathbf{k}} c_{i,\mathbf{k}+\mathbf{q}}^\dagger c_{i,\mathbf{k}} \quad (17)$$

and the response functions $\chi_{\tilde{\rho}\rho_i}, \chi_{\rho_i\rho_j}$ are defined analogously to $\chi_{\tilde{\rho}\tilde{\rho}}$ by Eq. (14). Eq. (16) corresponds to RPA which is given diagrammatically in Fig. 1.

One can easily reduce the infinite series in (16) to

$$\chi_{\tilde{\rho}\tilde{\rho}}^{\text{sc}} = \chi_{\tilde{\rho}\tilde{\rho}} + (\chi_{\tilde{\rho}\rho_1}, \chi_{\tilde{\rho}\rho_2}) (1 - U\chi)^{-1} U \begin{pmatrix} \chi_{\rho_1\tilde{\rho}} \\ \chi_{\rho_2\tilde{\rho}} \end{pmatrix}, \quad (18)$$

where 1 denotes the 2×2 unit matrix and we have defined the Coulomb interaction matrix

$$U = \begin{pmatrix} U_{11} & U_{12} \\ U_{21} & U_{22} \end{pmatrix} \quad (19)$$

and the real density response function matrix

$$\chi = \begin{pmatrix} \chi_{\rho_1\rho_1} & \chi_{\rho_1\rho_2} \\ \chi_{\rho_2\rho_1} & \chi_{\rho_2\rho_2} \end{pmatrix}. \quad (20)$$

In the continuum limit, the intralayer Coulomb interactions $U_{11} = U_{22} = \frac{2\pi e^2}{q_{\parallel}}$ and the interlayer Coulomb interactions $U_{12} = U_{21} = \frac{2\pi e^2}{q_{\parallel}} e^{-q_{\parallel}c}$ (q_{\parallel} is the momentum transfer parallel to a - b plane and c is the bilayer spacing [35]) which all go to infinity in the strong screening $q_{\parallel} \rightarrow 0$ limit. In the tight-binding strong-coupling limit, the couplings U_{ij} are themselves large. In either cases, one can approximate (18) by

$$\chi_{\tilde{\rho}\tilde{\rho}}^{\text{sc}} = \chi_{\tilde{\rho}\tilde{\rho}} - (\chi_{\tilde{\rho}\rho_1}, \chi_{\tilde{\rho}\rho_2}) \chi^{-1} \begin{pmatrix} \chi_{\rho_1\tilde{\rho}} \\ \chi_{\rho_2\tilde{\rho}} \end{pmatrix}. \quad (21)$$

The minus sign in (21) clearly exhibits the screening effect of the Coulomb interaction.

III. RESULTS AND DISCUSSIONS

Eqs. (13) and (21) allow one to study various symmetries of the *screened* Raman intensities for two-band systems. In this paper, however, we will focus on the c (or z) axis Raman intensities. We first specify the two uncoupled bands and the coupling:

$$\begin{aligned}\xi_1(k_x, k_y) &= \frac{\hbar^2}{2m}(k_x^2 + k_y^2) - \mu + \Delta \\ \xi_2(k_y) &= \frac{\hbar^2}{2m}k_y^2 - \mu \\ t(k_z) &= -2t_\perp \cos(k_z d/2),\end{aligned}\tag{22}$$

where Δ corresponds to the band splitting (responsible for the “pseudogap”), μ is the chemical potential, and t_\perp is the plane-chain coupling strength. While the bands ξ_1 and ξ_2 with circular and linear Fermi surface are used to simplify the calculation, they give qualitatively similar results to those given by more realistic tight-binding bands [9]. Since the k_z dependence only comes in through $t(k_z)$ which is assumed to have no k_x and k_y dependence, the only relevant geometry for the c -axis Raman spectra will be $(\hat{\mathbf{e}}^S, \hat{\mathbf{e}}^I) = (\hat{\mathbf{z}}, \hat{\mathbf{z}})$. Following (12), we define

$$\gamma_c(k_z) \equiv \begin{pmatrix} 0 & \gamma_{zz} \\ \gamma_{zz} & 0 \end{pmatrix},\tag{23}$$

where $\gamma_{zz} = (m/\hbar^2)\partial^2 t(k_z)/\partial k_z^2 = (t_\perp d^2 m/2\hbar^2)\cos(k_z d/2)$. Eq. (23) is the Raman vertex used in (10) for calculating the “ c -axis Raman intensities” throughout this paper.

In Appendix A, we have shown how one can separate all the response functions of Eq. (21) (needed in the calculation of the c -axis Raman spectra) into an *intraband* and an *interband* contributions. With these separations, one can easily estimate how each susceptibility χ depends on the coupling strength t_\perp , for both intraband and interband transitions. Of most interest, one sees that the unscreened Raman response function $\chi_{\tilde{\rho}\tilde{\rho}}$ has an intraband contribution which is proportional t_\perp^4 and an interband contribution which is proportional t_\perp^2 . Therefore, the interband transitions dominate for the unscreened c -axis Raman intensities when t_\perp is small.

In Fig. 2, we first show the *unscreened* Raman intensities for small $t_{\perp} = 2\text{meV}$ at different temperatures. Fixed parameters $\Delta = 20\text{meV}$ and $\mu = 500\text{meV}$ are used for all the results presented in this paper. To include the impurity scattering, we then introduce the scattering rates Γ_i into the Green's functions in (A6)

$$G_0^{-1}(\mathbf{k}, i\omega_n) = \begin{pmatrix} i\omega_n - \xi_1 + i\Gamma_1 \text{sgn}(\omega_n) & -t \\ -t & i\omega_n - \xi_2 + i\Gamma_2 \text{sgn}(\omega_n) \end{pmatrix}. \quad (24)$$

For simplicity, we will assume that the impurity scattering rates are equal for both bands ($\Gamma_1 = \Gamma_2 \equiv \Gamma$) and Γ is linear in temperature ($\Gamma = 20\text{meV}$ at $T = 100\text{K}$), but independent of frequency and momentum. As seen in Fig. 2, the c -axis Raman spectra can exhibit clear signatures of a pseudogap, as long as the temperature is not too high. At high temperatures for which $\Gamma \geq \Delta$, the pseudogap feature is washed out by the impurity broadening. This is, in particular, shown by the different low-frequency dependence of the intensities (see the inset in Fig. 2).

In Fig. 3, we present the $T = 20\text{K}$ unscreened Raman intensities for different coupling strengths. The inset shows that the unscreened c -axis Raman intensity can, in general, be separated into an intraband and an interband contribution. For better clarity of presentation, all intensities have been divided by t_{\perp}^2 . This leads to a almost constant interband contribution plus a intraband contribution proportional to t_{\perp}^2 . One finds at larger t_{\perp} that the pseudogap feature arising from the interband transitions are overwhelmed by the increasing contribution of intraband transitions which tend to dominate the Raman response.

We next consider the *screened* Raman intensity based on the full prescription of Eq. (21). Due to the Coulomb screening, the presence of the second (mixing) term in (21) results in the breakdown of the intraband and interband separation for the unscreened Raman intensity. For comparison with Figs. 2 and 3, we have presented in Figs. 4 and 5 the screened c -axis Raman intensities. Comparing Fig. 4 with Fig. 2, one sees no major difference between the unscreened and screened intensities except for different spectral weights of the higher-frequency intensity. This result is valid for the small- t_{\perp} case and can be established as follows. When t_{\perp} is small, one can ignore $\chi_{\rho_1\rho_2} \sim t_{\perp}^2$ in χ in (20) as compared to $\chi_{\rho_1\rho_1}, \chi_{\rho_2\rho_2}$

$\sim t_{\perp}^0$ (see Appendix A). Consequently, (21) can be reduced to a more elegant result

$$\chi_{\tilde{\rho}\tilde{\rho}}^{\text{sc}} = \chi_{\tilde{\rho}\tilde{\rho}} - \sum_{i=1}^2 \frac{(\chi_{\tilde{\rho}\rho_i})^2}{\chi_{\rho_i\rho_i}}. \quad (25)$$

That is, the screening effects can be separated for each layer. However, the complete separation of intraband and interband contributions is still not possible because the intra- and interband parts (both $\sim t_{\perp}^2$) of $\chi_{\tilde{\rho}\rho_i}$ are equally important (although $\chi_{\rho_i\rho_i} \sim t_{\perp}^0$ is dominated by the intraband transition). Nevertheless, the mixing (second) term in (25) is proportional to t_{\perp}^4 and has only a small effect when t_{\perp} is small. Therefore, the unscreened interband transition given by $\chi_{\tilde{\rho}\tilde{\rho}}$ still dominates. For higher values of t_{\perp} , as used in Figs. 5 and 3, the Coulomb screening has a large effect. In fact, in view of the inset in Fig. 5, the Coulomb screening effect tends to cancel against the unscreened interband contribution, largely leaving the unscreened intraband transition.

IV. CONCLUSIONS

In this paper, we have studied the c -axis Raman spectra such that both the incident and scattered photon polarizations are parallel to the \hat{z} -direction, for a plane-chain bilayer two-band cuprate. This coupled plane-chain model [9] has given a natural explanation of pseudogaps [11–13] seen in the AC c -axis optical conductivity. Here we have shown in detail how one can also study pseudogaps by doing c -axis Raman scattering. Our calculations are based on a tight-binding model for the Raman vertex. Coulomb screening effects are treated properly and include both intralayer and interlayer Coulomb interactions.

When the Coulomb screening is absent, the Raman intensity can be separated into an intraband and an interband contribution. The interband contribution ($\propto t_{\perp}^2$) dominates in the small- t_{\perp} limit. However, the presence of the Coulomb screening mixes up this separation and the resulting intensities are strongly dependent on the magnitude of t_{\perp} . Nevertheless, when t_{\perp} is small, the mixing effect arising from Coulomb screening is small and, as a result, the interband unscreened transition still dominates.

It's obvious that the approach derived in this paper for calculating Raman spectra in a two-band system can be easily extended to the case of a multiband system. A extension of our calculations of c -axis Raman intensities to the case of a superconducting plane-chain bilayer cuprate will be given elsewhere including the effect of impurities.

ACKNOWLEDGMENTS

We thank W.A. Atkinson and D. Branch for useful discussions. This work was supported by Natural Sciences and Engineering Research Council (NSERC) of Canada and Canadian Institute for Advanced Research (CIAR).

APPENDIX A: INTRABAND AND INTERBAND TRANSITIONS

In this appendix, we show how one can separate the response functions needed in the calculation of the Raman spectra into intraband and interband transitions. Consider a general response function

$$\chi_{AB}(\mathbf{q}, i\omega_n) = - \int_0^\beta d\tau e^{i\omega_n\tau} \langle T_\tau A_{\mathbf{q}}(\tau) B_{\mathbf{q}}^\dagger(0) \rangle, \quad (\text{A1})$$

where here, the operators A, B can be either the effective density $\tilde{\rho}$ or the real densities ρ_1 or ρ_2 . These operators can be written in a unified form such that in the limit $\mathbf{q} \rightarrow 0$

$$A = \sum_{\mathbf{k}} C_{\mathbf{k}}^\dagger \gamma(\mathbf{k}) C_{\mathbf{k}} = \sum_{\mathbf{k}} \sum_{i,j=1}^2 \gamma_{ij}^A c_{i,\mathbf{k}}^\dagger c_{j,\mathbf{k}}. \quad (\text{A2})$$

In (A2), the matrix γ is γ_c given in (23) for $\tilde{\rho}$ and

$$\gamma_1 = \begin{pmatrix} 1 & 0 \\ 0 & 0 \end{pmatrix} \text{ for } \rho_1 ; \quad \gamma_2 = \begin{pmatrix} 0 & 0 \\ 0 & 1 \end{pmatrix} \text{ for } \rho_2. \quad (\text{A3})$$

Using (A2), the average $\langle \dots \rangle$ in (A1) becomes

$$\begin{aligned} & \langle T_\tau A_{\mathbf{q}}(\tau) B_{\mathbf{q}}^\dagger(0) \rangle \\ &= \sum_{ijml=1}^2 \sum_{\mathbf{k}} \sum_{\mathbf{k}'} \gamma_{ij}^A(\mathbf{k}) \gamma_{ml}^B(\mathbf{k}') \langle T_\tau c_{i,\mathbf{k}}^\dagger(\tau) c_{j,\mathbf{k}}(\tau) c_{m,\mathbf{k}'}^\dagger(0) c_{l,\mathbf{k}'}(0) \rangle \end{aligned}$$

$$\begin{aligned}
&= - \sum_{ijml=1}^2 \sum_{\mathbf{k}} \sum_{\mathbf{k}'} \gamma_{ij}^A(\mathbf{k}) \gamma_{ml}^B(\mathbf{k}') \langle T_\tau c_{l,\mathbf{k}}(0) c_{i,\mathbf{k}'}^\dagger(\tau) \rangle \langle T_\tau c_{j,\mathbf{k}}(\tau) c_{m,\mathbf{k}'}^\dagger(0) \rangle \\
&= - \sum_{ijml=1}^2 \sum_{\mathbf{k}} \gamma_{ij}^A(\mathbf{k}) \gamma_{ml}^B(\mathbf{k}) G_{li}^0(\mathbf{k}, -\tau) G_{jm}^0(\mathbf{k}, \tau).
\end{aligned} \tag{A4}$$

The development from the second to the third line in (A4) makes use of the usual Hartree-Fock approximation. G_{ij}^0 are the elements of a 2×2 non-interacting Green's function matrix defined by

$$G_0(\mathbf{k}, \tau) = -\langle T_\tau C_{\mathbf{k}}(\tau) C_{\mathbf{k}}^\dagger(0) \rangle. \tag{A5}$$

For the present coupled plane-chain bilayer model, one has (see (3))

$$G_0^{-1}(\mathbf{k}, i\omega_n) = \begin{pmatrix} i\omega_n - \xi_1 & -t \\ -t & i\omega_n - \xi_2 \end{pmatrix}. \tag{A6}$$

Substituting (A4) into (A1) and making use of the Fourier transform

$$G_{ij}^0(\mathbf{k}, \tau) = \frac{1}{\beta} \sum_{i\omega_{n'}} e^{-i\omega_{n'}\tau} G_{ij}^0(\mathbf{k}, i\omega_{n'}) \tag{A7}$$

and the orthogonal relation

$$\frac{1}{\beta} \int_0^\beta d\tau e^{i(\omega_n - \omega_{n'})\tau} = \delta_{\omega_n, \omega_{n'}}, \tag{A8}$$

one obtains

$$\chi_{AB}(\mathbf{q} \rightarrow 0, i\omega_n) = \frac{1}{\beta} \sum_{\omega_{n'}} \sum_{\mathbf{k}} \sum_{ijml=1}^2 \gamma_{ij}^A(\mathbf{k}) \gamma_{ml}^B(\mathbf{k}) G_{li}^0(\mathbf{k}, i\omega_{n'}) G_{jm}^0(\mathbf{k}, i\omega_{n'} + i\omega_n). \tag{A9}$$

Furthermore, using (23), (A3), and the fact that $G_{12}^0 = G_{21}^0$, one finds

$$\begin{aligned}
\chi_{\tilde{\rho}\tilde{\rho}} &= \frac{1}{\beta} \sum_{\omega_{n'}} \sum_{\mathbf{k}} \text{Tr}[G_0(\mathbf{k}, i\omega_{n'}) \gamma_c G_0(\mathbf{k}, i\omega_{n'} + i\omega_n) \gamma_c] \\
\chi_{\tilde{\rho}\rho_i} &= \chi_{\rho_i \tilde{\rho}} = \frac{1}{\beta} \sum_{\omega_{n'}} \sum_{\mathbf{k}} \text{Tr}[G_0(\mathbf{k}, i\omega_{n'}) \gamma_c G_0(\mathbf{k}, i\omega_{n'} + i\omega_n) \gamma_i] \\
\chi_{\rho_i \rho_j} &= \chi_{\rho_j \rho_i} = \frac{1}{\beta} \sum_{\omega_{n'}} \sum_{\mathbf{k}} \text{Tr}[G_0(\mathbf{k}, i\omega_{n'}) \gamma_i G_0(\mathbf{k}, i\omega_{n'} + i\omega_n) \gamma_j].
\end{aligned} \tag{A10}$$

The trace operator enables one to calculate $\chi_{\tilde{\rho}\tilde{\rho}}$, etc in (A10) in any rotated frame which is convenient. We will choose a frame in which the Green's function matrix is diagonal. This leads to results that are readily interpretable physically (see later).

We first diagonalize the Hamiltonian h in (3) and the Green's function matrix G_0^{-1} in (A6)

$$h(\mathbf{k}) \rightarrow \hat{h}(\mathbf{k}) = U^\dagger(\mathbf{k})h(\mathbf{k})U(\mathbf{k}) = \begin{pmatrix} \epsilon_+ & 0 \\ 0 & \epsilon_- \end{pmatrix},$$

$$G_0^{-1} \rightarrow \hat{G}_0^{-1} = U^\dagger G_0^{-1} U = \begin{pmatrix} i\omega_n - \epsilon_+ & 0 \\ 0 & i\omega_n - \epsilon_- \end{pmatrix}, \quad (\text{A11})$$

where the unitary matrix is

$$U(\mathbf{k}) = \frac{1}{\sqrt{\epsilon_+ - \epsilon_-}} \begin{pmatrix} -\frac{t}{|t|}\sqrt{\xi_1 - \epsilon_-} & -\frac{t}{|t|}\sqrt{\epsilon_+ - \xi_1} \\ -\sqrt{\epsilon_+ - \xi_1} & \sqrt{\xi_1 - \epsilon_-} \end{pmatrix} \quad (\text{A12})$$

and the eigenvalues are

$$\epsilon_\pm = \frac{\xi_1 + \xi_2}{2} \pm \sqrt{\left(\frac{\xi_1 - \xi_2}{2}\right)^2 + t^2}. \quad (\text{A13})$$

In an analogous way, one can rotate the vertices

$$\gamma_c \rightarrow \hat{\gamma}_c = U^\dagger \gamma_c U = \frac{\gamma_{zz}}{\epsilon_+ - \epsilon_-} \begin{pmatrix} 2t & -\frac{t}{|t|}(\xi_1 - \xi_2) \\ -\frac{t}{|t|}(\xi_1 - \xi_2) & -2t \end{pmatrix}, \quad (\text{A14})$$

$$\gamma_1 \rightarrow \hat{\gamma}_1 = U^\dagger \gamma_1 U = \frac{1}{\epsilon_+ - \epsilon_-} \begin{pmatrix} \xi_1 - \epsilon_- & |t| \\ |t| & \epsilon_+ - \xi_1 \end{pmatrix}, \quad (\text{A15})$$

and

$$\gamma_2 \rightarrow \hat{\gamma}_2 = U^\dagger \gamma_2 U = \frac{1}{\epsilon_+ - \epsilon_-} \begin{pmatrix} \epsilon_+ - \xi_1 & -|t| \\ -|t| & \xi_1 - \epsilon_- \end{pmatrix}. \quad (\text{A16})$$

For convenience, we redefine

$$\hat{G}_0 = \begin{pmatrix} G_{11} & 0 \\ 0 & G_{22} \end{pmatrix}, \quad \hat{\gamma}_c = \begin{pmatrix} \gamma_{11} & \gamma_{12} \\ \gamma_{12} & -\gamma_{11} \end{pmatrix},$$

$$\hat{\gamma}_1 = \begin{pmatrix} \alpha_{11} & \alpha_{12} \\ \alpha_{12} & \alpha_{22} \end{pmatrix}, \quad \hat{\gamma}_2 = \begin{pmatrix} \alpha_{22} & -\alpha_{12} \\ -\alpha_{12} & \alpha_{11} \end{pmatrix}, \quad (\text{A17})$$

where one can easily identify these new variables. Substituting (A17) into (A10), we obtain

$$\begin{aligned}
\chi_{\bar{\rho}\bar{\rho}} &= \frac{1}{\beta} \sum_{\omega_{n'}} \sum_{\mathbf{k}} \gamma_{11}^2 (G_{11}G'_{11} + G_{22}G'_{22}) + \gamma_{12}^2 (G_{11}G'_{22} + G_{22}G'_{11}), \\
\chi_{\bar{\rho}\rho_1} &= \chi_{\rho_1\bar{\rho}} = \frac{1}{\beta} \sum_{\omega_{n'}} \sum_{\mathbf{k}} \gamma_{11} (\alpha_{11}G_{11}G'_{11} - \alpha_{22}G_{22}G'_{22}) + \gamma_{12}\alpha_{12} (G_{11}G'_{22} + G_{22}G'_{11}), \\
\chi_{\bar{\rho}\rho_2} &= \chi_{\rho_2\bar{\rho}} = \frac{1}{\beta} \sum_{\omega_{n'}} \sum_{\mathbf{k}} \gamma_{11} (\alpha_{22}G_{11}G'_{11} - \alpha_{11}G_{22}G'_{22}) - \gamma_{12}\alpha_{12} (G_{11}G'_{22} + G_{22}G'_{11}), \\
\chi_{\rho_1\rho_1} &= \frac{1}{\beta} \sum_{\omega_{n'}} \sum_{\mathbf{k}} (\alpha_{11}^2 G_{11}G'_{11} + \alpha_{22}^2 G_{22}G'_{22}) + \alpha_{12}^2 (G_{11}G'_{22} + G_{22}G'_{11}), \\
\chi_{\rho_2\rho_2} &= \frac{1}{\beta} \sum_{\omega_{n'}} \sum_{\mathbf{k}} (\alpha_{22}^2 G_{11}G'_{11} + \alpha_{11}^2 G_{22}G'_{22}) + \alpha_{12}^2 (G_{11}G'_{22} + G_{22}G'_{11}), \\
\chi_{\rho_1\rho_2} &= \chi_{\rho_2\rho_1} = \frac{1}{\beta} \sum_{\omega_{n'}} \sum_{\mathbf{k}} \alpha_{11}\alpha_{22} (G_{11}G'_{11} + G_{22}G'_{22}) - \alpha_{12}^2 (G_{11}G'_{22} + G_{22}G'_{11}), \tag{A18}
\end{aligned}$$

where $G \equiv G(\mathbf{k}, i\omega_{n'})$ and $G' \equiv G(\mathbf{k}, i\omega_{n'} + i\omega_n)$. Clearly for each χ in (A18), the first term corresponds to an *intraband* contribution and the second term corresponds to an *interband* contribution. Crudely speaking, when t_\perp is small (recall (22) and (23)), $\gamma_{11} \sim t_\perp^2$, $\gamma_{12} \sim t_\perp^1$, $\alpha_{11} \sim t_\perp^0$, $\alpha_{22} \sim t_\perp^2$, and $\alpha_{12} \sim t_\perp^1$. These in turn allow one to estimate the t_\perp -dependence of each χ , for both intraband and interband transitions.

APPENDIX B: PLANE-PLANE BILAYER MODEL

In this Appendix, we present the analogous results for the c -axis Raman intensities in a coupled plane-plane bilayer. Due to the identity of these two layers, analytical results are available and hence gives more insight into the numerical results of the plane-chain model. Similar to Eq. (22), we use the simple bands

$$\begin{aligned}
\xi_1(k_x, k_y) &= \frac{\hbar^2}{2m} (k_x^2 + k_y^2) - \mu + \Delta \\
\xi_2(k_x, k_y) &= \frac{\hbar^2}{2m} (k_x^2 + k_y^2) - \mu, \tag{B1}
\end{aligned}$$

for the two planes which are separated by a band gap Δ (pseudogap). The coupling between these two planes is the same as given in (22). In the case of small t_\perp , one can approximate $\epsilon_+ = \xi_1$ and $\epsilon_- = \xi_2$ (see (A13)).

With the above simplification, the unscreened c -axis Raman intensity given by the imaginary part of $\chi_{\bar{\rho}\bar{\rho}}$ in (A18) can easily be worked out to be proportional to

$$t_{\perp}^2 \omega \left[\frac{6t_{\perp}^2}{\Delta^2} \frac{4\Gamma}{(\hbar\omega)^2 + 4\Gamma^2} + \left(\frac{2\Gamma}{(\hbar\omega + \Delta)^2 + 4\Gamma^2} + \frac{2\Gamma}{(\hbar\omega - \Delta)^2 + 4\Gamma^2} \right) \right], \quad (\text{B2})$$

where the first term corresponds to the familiar intraband transition ($\propto t_{\perp}^4$) and the second term corresponds to the interband transition ($\propto t_{\perp}^2$). One can see from (B2) that apart from the prefactor $t_{\perp}^2 \omega$, the interband term contains the same factors as the intraband term except for a peak shift from $\omega = 0$ to $\omega = \pm\Delta$ in the Lorentzian form. At zero frequency the first Drude like contribution in (B2) will go like $6t_{\perp}^2/\Delta^2\Gamma$ while the second (interband) term will go instead like $4\Gamma/\Delta^2$ which is the opposite dependence on Γ than exhibited by the first term. Also for $t_{\perp} \rightarrow 0$ the Drude term is small compared with the second term which will then exhibit a pseudogap for $\hbar\omega \lesssim \Delta$ as $\Gamma \rightarrow 0$. Using (B2), we plot in Fig. 6 the temperature-dependent c -axis Raman intensities for the plane-plane bilayer model. All the parameters used are the same as those used in Fig. 2. It is seen in Fig. 6 that a pseudogap can develop in the c -axis Raman intensities at low frequencies provided the temperature (or the impurity damping rate Γ) is not too high. We remark that, in analogy to the plane-chain case, the Coulomb screening has little effect on the small- t_{\perp} unscreened intensities given in Fig. 6.

The major difference between the results in Fig. 2 for a plane-chain bilayer and those in Fig. 6 for a plane-plane bilayer is that the spectral weight just beyond the pseudogap frequency is much higher in the former case than in the latter case. This can be explained as follows. For a plane-plane bilayer in which the two bands are separated by a constant band gap (Δ) all over the Brillouin zone, the interband transitions will be peaked at $\omega = \Delta$. In contrast in the plane-chain bilayer, the band gap between the plane and chain bands varies at different \mathbf{k} points (with minimum value of Δ) and, as a result, the interband transitions are spreaded out for $\omega \geq \Delta$.

REFERENCES

- [1] S. L. Copper and K. E. Gray, in *Physical Properties of High Temperature Superconductors IV*, edited by D. M. Ginsberg (World Scientific, Singapore, 1994), p. 61.
- [2] C. C. Homes, T. Timusk, R. Liang, D. A. Bonn, and W. N. Hardy, *Phys. Rev. Lett.* **71**, 1645 (1993).
- [3] C. C. Homes, T. Timusk, D. A. Bonn, R. Liang, and W. N. Hardy, *Physica C* **254**, 265 (1995).
- [4] Y. Zha, S. L. Copper, and D. Pines, *Phys. Rev. B* **53**, 8253 (1996).
- [5] M. J. Graf, D. Rainer, and J. A. Sauls, *Phys. Rev. B* **47**, 12089 (1993).
- [6] A. G. Rojo and K. Levin, *Phys. Rev. B* **48**, 16861 (1993).
- [7] N. Kumar and A. M. Jayannavar, *Phys. Rev. B* **45**, 5001 (1992).
- [8] A. J. Leggett, *Braz. J. Phys.* **22**, 129 (1992).
- [9] W. A. Atkinson and J. P. Carbotte, *Phys. Rev. B*, in press.
- [10] W. C. Wu, W. A. Atkinson, and J. P. Carbotte, unpublished.
- [11] D. N. Basov *et al.*, *Phys. Rev. Lett.* **74**, 598 (1995).
- [12] A. V. Puchkov, D. N. Basov, and T. Timusk, preprint.
- [13] Y. W. Hsueh, B. W. Statt, M. Reedyk, T. Timusk, J. S. Xue, and J. E. Greedan, preprint.
- [14] A. A. Maksimov, A. V. Puchkov, and I. I. Tartakovskii, *Solid State Commun.* **81**, 407 (1992).
- [15] M. Boekholt, A. Hoffmann, and G. Güntherodt, *Physica C* **175**, 127 (1991).
- [16] D. Reznik *et al.*, *Phys. Rev. B* **48**, 7624 (1994).

- [17] X. K. Chen, E. Altendorf, J. C. Irwin, R. Liang, and W. N. Hardy, Phys. Rev. B **48**, 10530 (1993).
- [18] T. Staufer, R. Newetchek, R. Hackl, P. Müller, and H. Veith, Phys. Rev. Lett. **68**, 1069 (1992).
- [19] X. K. Chen, R. Liang, W. Hardy, and J. C. Irwin, J. Supercond. **7**, 435 (1994).
- [20] X. K. Chen, J. C. Irwin, R. Liang, and W. Hardy, Physica C **227**, 113 (1994).
- [21] T. P. Devereaux, D. Einzel, B. Stadlober, and R. Hackl, Phys. Rev. Lett. **72**, 3291 (1994).
- [22] A. Hoffmann, P. Lemmens, G. Güntherodt, V. Thomas, and K. Winzer, Physica C **235-240**, 1897 (1994).
- [23] A. Hoffmann, P. Lemmens, L. Winkeler, and G. Güntherodt, J. Low Temp. Phys. **99**, 201 (1995).
- [24] C. Kendziora and A. Rosenberg, Phys. Rev. B **52**, R9867 (1995).
- [25] X. K. Chen, J. C. Irwin, H. J. Trodahl, T. Kimura, and K. Kishio, Phys. Rev. Lett. **73**, 3290 (1994).
- [26] D. Branch and J. P. Carbotte, Phys. Rev. B **52**, 603 (1995).
- [27] D. Branch and J. P. Carbotte, Phys. Rev. B **54**, 13288 (1996).
- [28] T. P. Devereaux, A. Virosztek, and A. Zawadowski, Phys. Rev. B **54**, 12523 (1996).
- [29] W. A. Atkinson and J. P. Carbotte, Phys. Rev. B **52**, 10601 (1995).
- [30] G. D. Mahan, *Many-Particle Physics*, second edition (Plenum, New York, 1990), p. 777.
- [31] A. A. Abrikosov and V. M. Genkin, Sov. Phys.-JETP **38**, 417 (1974).
- [32] M. V. Klein and S. B. Dierker, Phys. Rev. B **29**, 4976 (1984).

[33] H. Monien and A. Zawadowski, Phys. Rev. B **41**, 8798 (1990).

[34] T. P. Devereaux *et al.*, Phys. Rev. Lett. **72**, 396 (1994).

[35] See, for example, A. Griffin and A. J. Pindor, Phys. Rev. B **39**, 11503 (1989).

FIGURES

$$\chi^{\text{sc}} = \begin{array}{c} \chi \\ \text{Diagram 1} \end{array} + \begin{array}{c} \text{Diagram 2} \end{array} + \begin{array}{c} \text{Diagram 3} \end{array} + \dots$$

FIG. 1. Diagrams for the screened Raman response function. Each interaction line comprises four parts corresponding to intralayer and interlayer Coulomb interactions.

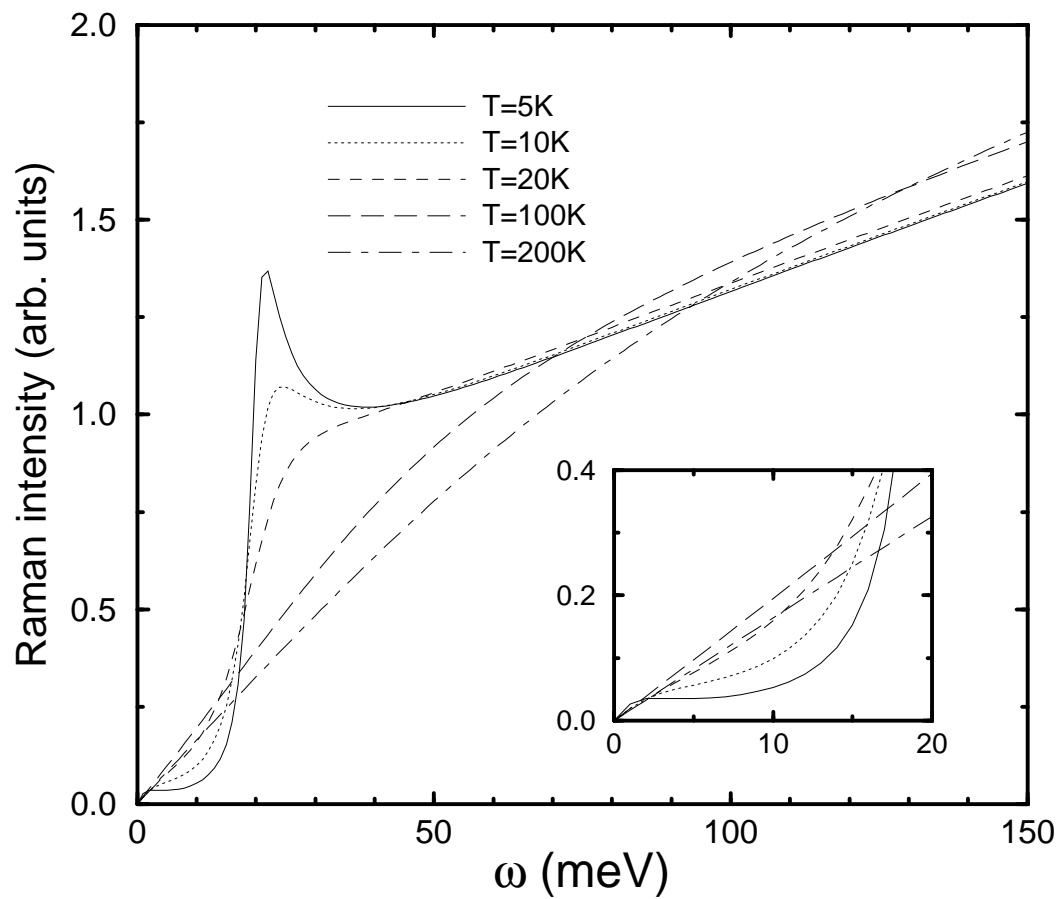


FIG. 2. Unscreened c -axis Raman intensities for $t_{\perp} = 2\text{meV}$ at various temperatures. We magnify in the inset the different ω -dependence of the low-frequency intensities.

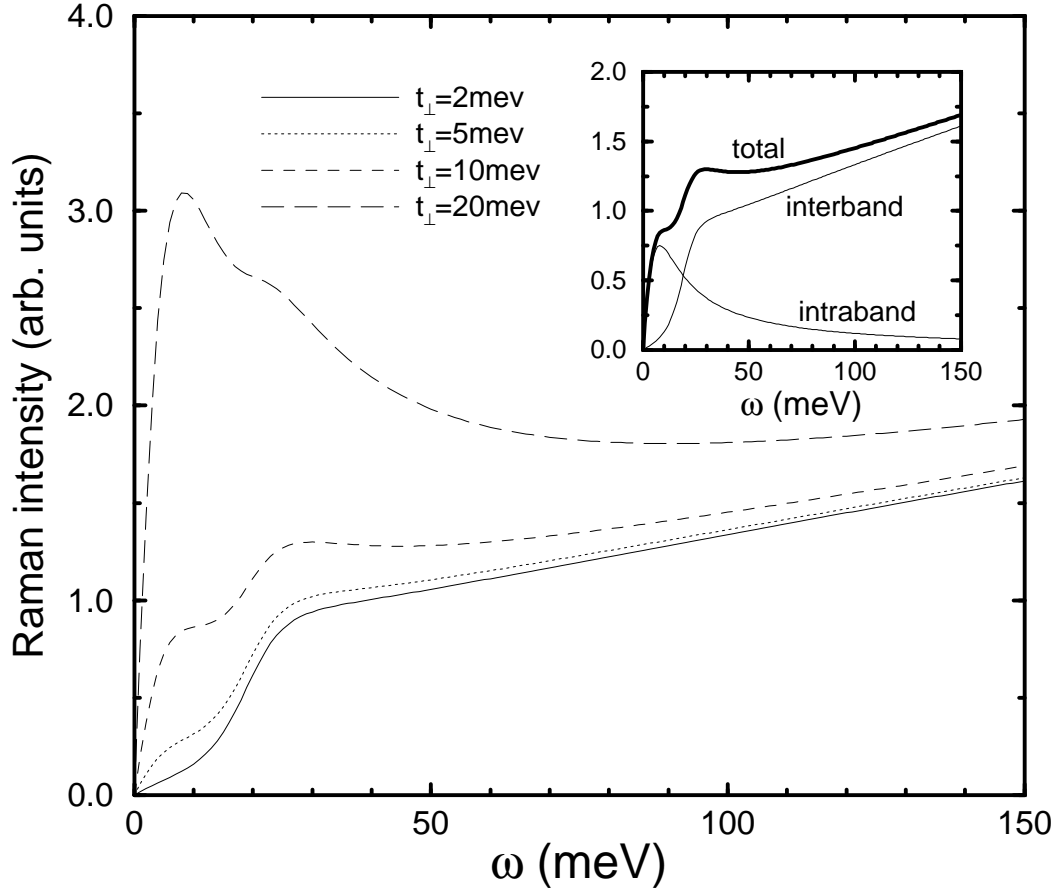


FIG. 3. Unscreened c -axis Raman intensities at $T = 20K$ with different values of plane-chain coupling t_{\perp} . For easier comparison, all intensities are divided by t_{\perp}^2 . The inset shows the separation into intraband and interband transitions of the unscreened c -axis Raman intensity (for the $t_{\perp} = 10\text{meV}$ case).

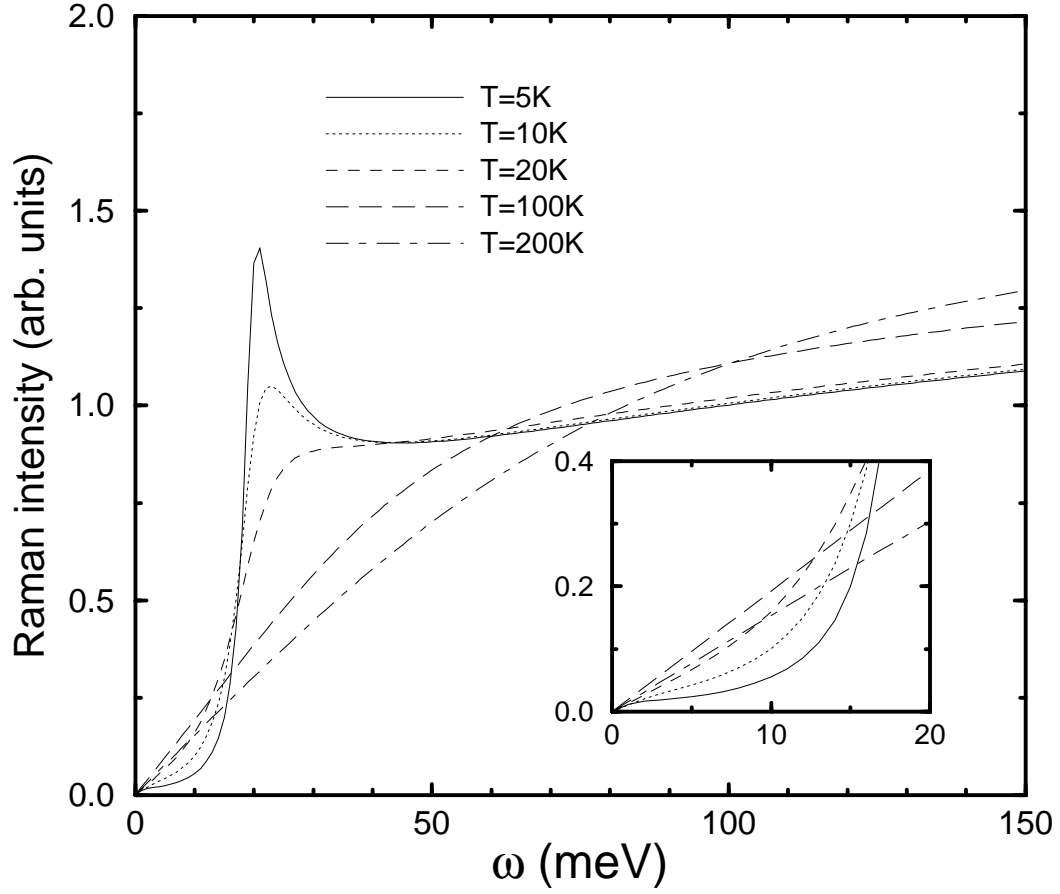


FIG. 4. Screened c -axis Raman intensities for $t_{\perp} = 2\text{meV}$ at various temperatures (to be compared to Fig. 2).

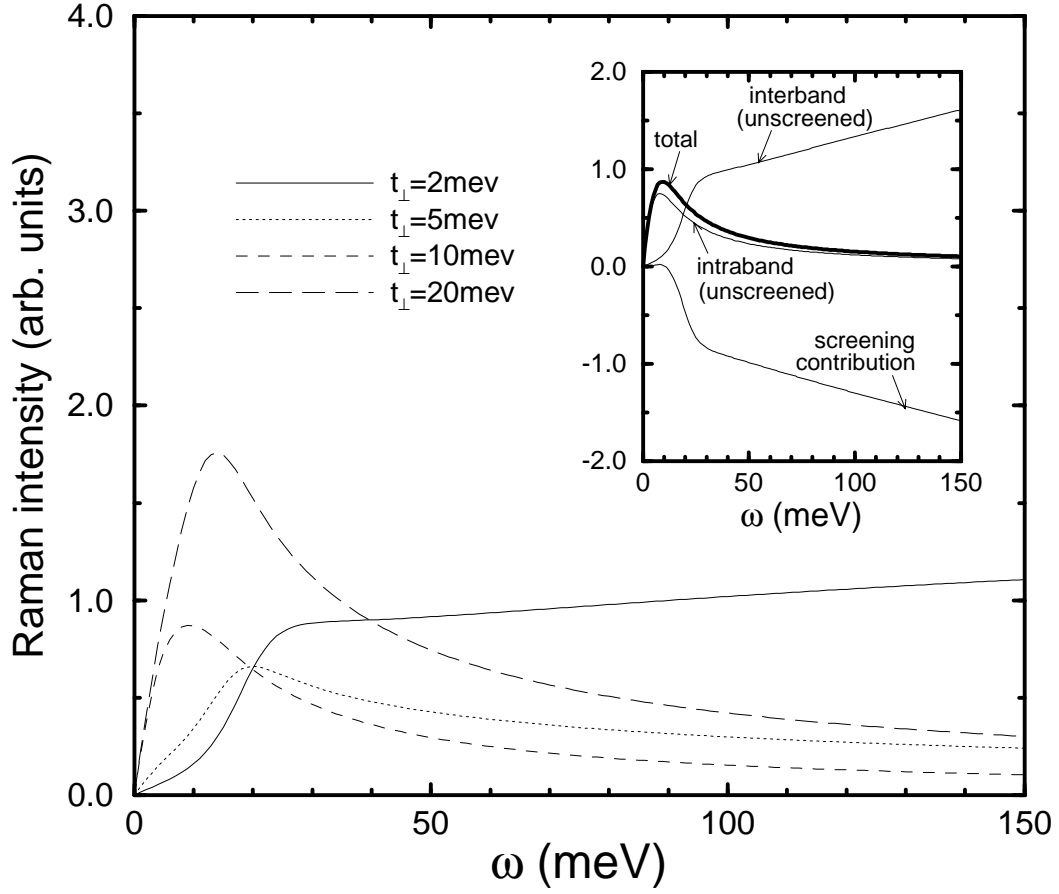


FIG. 5. Screened c -axis Raman intensities at $T = 20K$ for various values of t_{\perp} (to be compared to Fig. 3). The inset (for $t_{\perp} = 10\text{meV}$) shows separately the three different contributions, namely the unscreened intraband, unscreened interband, and screening effect.

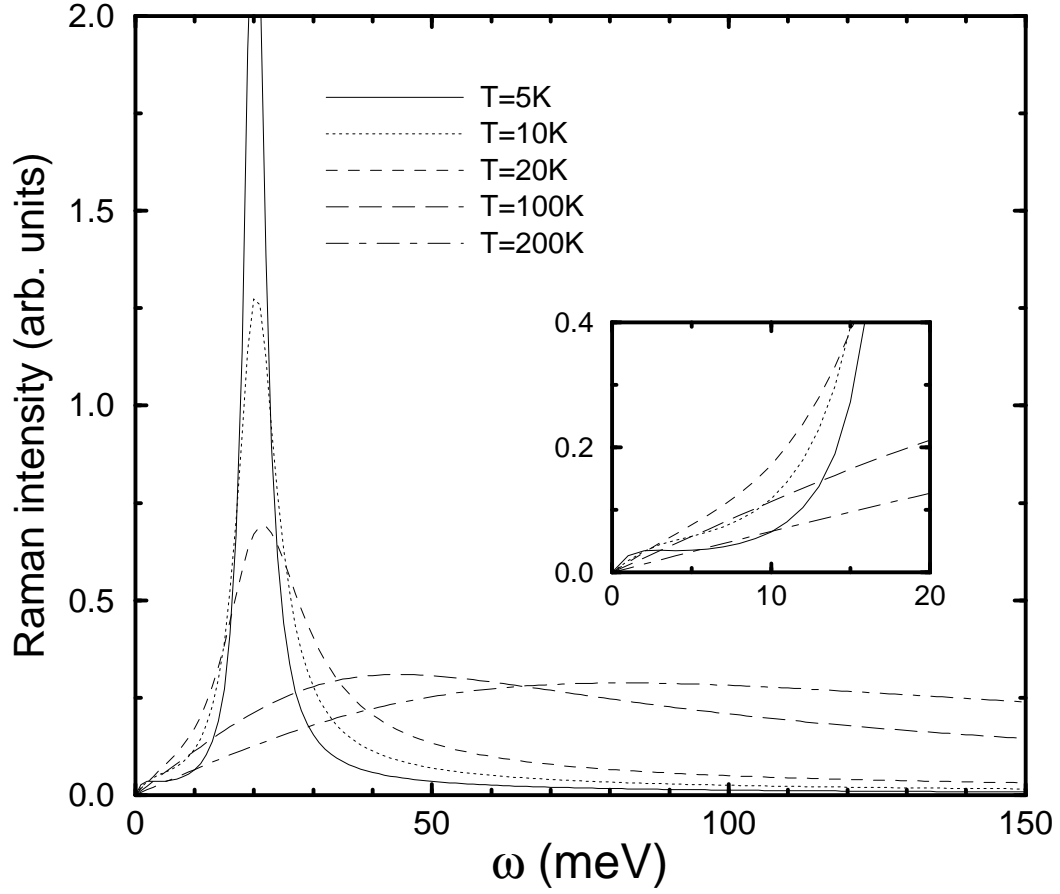


FIG. 6. Unscreened c -axis Raman intensities in a coupled plane-plane bilayer model for $t_{\perp} = 2\text{meV}$ at various temperatures. The inset shows the different low-frequency ω -dependence of the intensities. This is to be compared with Fig. 2 which applies to the plane-chain bilayer.